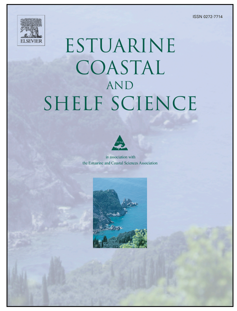

Shoreline dynamics of the active Yellow River delta since the implementation of Water-Sediment Regulation Scheme: A remote-sensing and statistics-based approach

Yaoshen Fan, Shenliang Chen, Bo Zhao, Shunqi Pan, Chao Jiang, Hongyu Ji

PII: S0272-7714(17)30866-1

DOI: 10.1016/j.ecss.2017.11.035

Reference: YECSS 5692

To appear in: *Estuarine, Coastal and Shelf Science*

Received Date: 30 August 2017

Revised Date: 21 November 2017

Accepted Date: 28 November 2017

Shoreline dynamics of the active Yellow River delta since the implementation of Water-Sediment Regulation Scheme: A remote-sensing and statistics-based approach

Yaoshen Fan [a], Shenliang Chen [a,*], Bo Zhao [b], Shunqi Pan [c], Chao Jiang [a], Hongyu Ji [a]

[a] State Key Laboratory of Estuarine and Coastal Research, East China Normal University, Shanghai 200062, China

[b] College of Earth, Ocean, and Atmospheric Sciences, Oregon State University, Corvallis, 97331 USA

[c] Hydro-environmental Research Centre, School of Engineering, Cardiff University, Cardiff CF24 3AA, UK

[*]Corresponding author.

Tel: +86 (0)21-62233686

Email address: slchen@sklec.ecnu.edu.cn (S.L. Chen)

Abstract: The Active Yellow River (Huanghe) Delta (AYRD) is a complex landform in which rapid deposition takes place due to its geologic formation and evolution. Continuous monitoring of shoreline dynamics at high-temporal frequency is crucial for understanding the processes and the driving factors behind this rapidly changing coast. Great efforts have been devoted to map the changing shoreline of the Yellow River delta and explain such changes through remote sensing data. However, the temporal frequency of shoreline in the obtained datasets are generally not fine enough to reflect the detailed or subtly variable processes of shoreline retreat and advance. To overcome these limitations, we continuously monitored the dynamics of this shoreline using time series of Landsat data based on tidal-level calibration model and orthogonal-transect method. The Abrupt Change Value (ACV) results indicated that the retreat-advance patterns had a significant impact regardless of season or year. The Water-Sediment Regulation Scheme (WSRS) plays a dominant role in delivering river sediment discharge to the sea and has an impact on the annual average maximum ACV, especially at the mouth of the river. The positive relationship among the average ACV, runoff and sediment load are relatively obvious; however, we found that the Relative Exposure Index (REI) that measures wave energy was able to explain only approximately 20 % of the variation in the data. Based on the abrupt change at the shoreline of the AYRD, river flow and time, we developed a binary regression model to calculate the critical sediment load and water discharge for maintaining the equilibrium of the active delta from 2002 to 2015. These values were approximately 0.48×10^8 t/yr and 144.37×10^8 m^3/yr. If the current water and sediment proportions released from the Xiaolangdi Reservoir during the WSRS remain stable, the erosion-accretion patterns of the active delta will shift from rapid accretion to a dynamic balance.

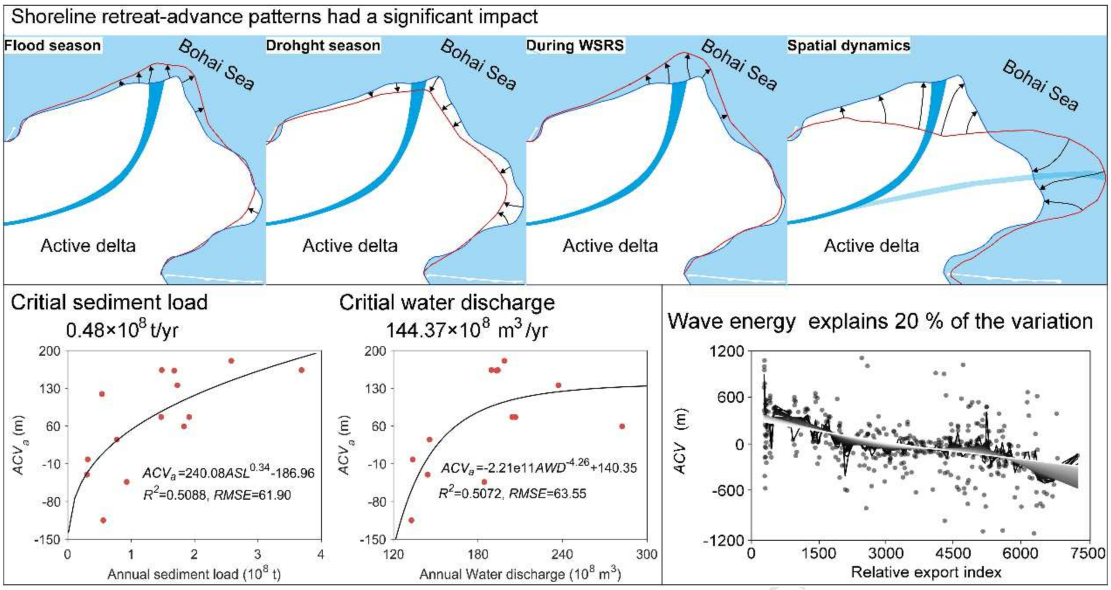

Keywords: Active Yellow River delta; Shoreline dynamics; The Water-Sediment Regulation Scheme; River input; Wave energy

1. Introduction

The shoreline represents a highly dynamic physical interface between land and water (Boak and Turner, 2005; Dolan et al., 1980), and shoreline position is recognized by the International Geographic Data Committee (IGDC) as one of the twenty-seven features (Berger and Iams, 1996; Mujabar and Chandrasekar, 2013). Due to the effects of global warming and sea-level rise, shorelines worldwide have tended to retreat (Dar and Dar, 2009). Marine processes such as wind, waves and tidal currents are major factors affecting coastal dynamics. Waves impacting the shoreline can suspend sediment while currents can transport these materials elsewhere, causing erosion. The threat of erosion is higher in areas with larger fetches due to greater anticipated wave buildup (Phillips, 1986). Delta shoreline change is susceptible not only to adjacent coasts but also to human activities in the drainage area. Over the past century, sediment loads of many rivers have decreased because of damming and irrigation, as well as improved land-use practices, thereby triggering coastal erosion of many deltas (Milliman, 1997; Syvitski et al., 2009), including those of the Nile (Fanos, 1995; Ali and El-Magd, 2016), Colorado (Carriquiry et al., 2001), Mississippi (Blum and Roberts, 2009), Ebro (Sánchez-Arcilla et al., 1998), Godavari and Krishna (Rao al., 2010), Mekong (Anthony et al., 2015), Yangtze (Yang et al., 2011; Song et al., 2015; Du et al., 2016), and Yellow (Chu et al., 2006; Wang et al., 2007; Xu, 2008; Bi et al., 2014; Jiang et al, 2017) rivers. Therefore, monitoring shoreline dynamics is crucial, since it provides essential information for understanding coastal response to contemporary climate change and other human impacts (Jones et al., 2009; Maiti and Bhattacharya, 2009).

Compared to conventional survey methods, remote sensing has the advantage of being able to monitor shoreline dynamics on a variety of spatial-temporal scales (Rao et al., 1985; Jangir et al., 2016; Gens, 2010). Determining accurate trends from various shoreline positions has been a subject of considerable interest (Dewi et al, 2016). Though it is strictly defined as the intersection of water and land surfaces, for practical purposes, the dynamic nature of shorelines and its dependence on the temporal and spatial scale at which it is being considered results in the use of a range of shoreline indicators (Boak and Turner, 2005). These proxies fall into two categories: either a feature that is visibly discernible in coastal imagery (Murray et al., 2014; Pardo-Pascual et al., 2012; Rahman et al., 2011) or one that can be observed via the intersection of tidal datum with the coastal profile (Morton, 1998; Chen et al., 2009; Liu et al., 2013a; Khomsin, 2017). Apparently, the latter is more suitable for tidal areas. This is particularly true for coasts with gentle slopes. Though river delta shoreline changes are always discontinuous due to the presence of channels, objective criteria for them have been delineated via image processing methods, including dilation and erosion operators of mathematical morphology (Geleynse et al., 2012), opening angle method (Shaw et al., 2008) and fuzzy classification (Dewi et al., 2016). Compared to some long-term monitoring studies (Ekercin, 2007; Li et al., 2014; Karsli, et al., 2011; Choung and Jo, 2016), detecting shoreline changes annually via Landsat data has increased the monitoring temporal frequency and improved our understanding of each driving factor's contribution (Gratiot et al., 2008; Li and Gong, 2015; Xu and Gong, 2016).

The AYRD is one of the most poignant examples worldwide of the huge impacts of frequent flooding, river course shifts and human activities affecting water consumption, river regulation, soil and water conservation, etc. (Liu et al., 2014b). The purpose of the Water-Sediment Regulation Scheme (WSRS), installed in 2002, at the Xiaolangdi (XLD) Reservoir is to control flooding, maintain the reservoir capacity and scour the elevated river-bed in the lower Yellow River. Over the past 30 years, many studies have been carried out on the AYRD to access its social economic value and unique ecosystem (Cui et al., 2009). Researchers have primarily focused on the relationship between the evolution of the delta and the stream-flow and sediment load in the delta (Peng et al., 2010b; Wang et al., 2010; Yu et al., 2011; Kong et al., 2015a), land-use near this region (Zhang et al., 2011; Ottinger et al., 2013; Sui et al., 2015), and long-term changes of the delta shoreline (Cui and Li, 2011; Kuenzer et al., 2014). Under the influence of XLD Reservoir and WSRS on seasonal distribution of water and sediment, less attention has been paid to temporal and spatial variability on the active delta shoreline seasonally or event scales (water-sediment regulation event) and their relationship to the river influx and marine dynamics.

Therefore, the main objectives of this study are follows: (1) to find a more suitable delta shoreline indicator based on intertidal slope, estimated from two Landsat datasets:(2) to establish a high temporal resolution shoreline map using time series satellite images: (3) to quantify seasonal shoreline changes of AYRD since the implementation of WSRS; and (4) to further discuss how sediment load and coastal relative exposure index (REI) are related to changes of the shoreline.

2. Study area and background

2.1 Yellow River and active Yellow River Delta

The 5,464 km-long Yellow River originates from the northern Qinghai-Tibetan Plateau and discharges into the Bohai Sea (Fig. 1a), draining an area of approximately 742, 400 km^2 which comprises both semi-arid and semi-humid climatic zones. Its upper reaches (from the headwater to Toudaoguai (TDG)) drain into the northern Qinghai-Tibetan Plateau and provide approximately 60% of the river's water discharge. The middle reaches of the Yellow River (from the TDG to the Huayuankou (HYK)) cross the Loess Plateau, which is very lush and prone to erosion during rain storms. The river gains 90 % of its sediment load during this journey.

The Yellow River delta is normally referred to as the "fan-shaped" area, in which

Ninghai town serves as the axis of change in flow, upstream of which, the course is more stable. Downstream from Ninghai lies an area of approximately 6,000 km^2 extending from the mouth of the Taoerhe to the north and to the mouth of the Zhimaigou to the south (Figure 1b). The river's course has been radically changed eleven times in the deltaic region from 1855 to the present, including four intentional flood control measures in 1953, 1964, 1976 and 1996. The latest change was artificially created in 1996, resulting in a shift in the main channel northwards from the Qingshuigou course to Q8, which ultimately led to the formation of a delta. The Qingshuigou course was marked as "abandoned course," as shown in Figure 1c.

Since 1996, the AYRD has become a complexly evolving rapid deposition body. Due to the changes of riverine and coastal dynamics, the downstream end of the Q8 course shifted naturally in 2007 and forced the channel northward to the Bohai Sea. These rapid changes, most likely as a result of climate change, have significantly impacted the hydrodynamic conditions of this mega-delta. For this reason, we chose to investigate these complex processes via the field measurements, high-resolution remote-sensing images, and hydrographic measurements at Lijin Station. Due to the typical curvilinear nature of the bars and islands within the delta, we decided to focus on the entire current active delta between Groin A and Groin B, as indicated in Figure 1c.

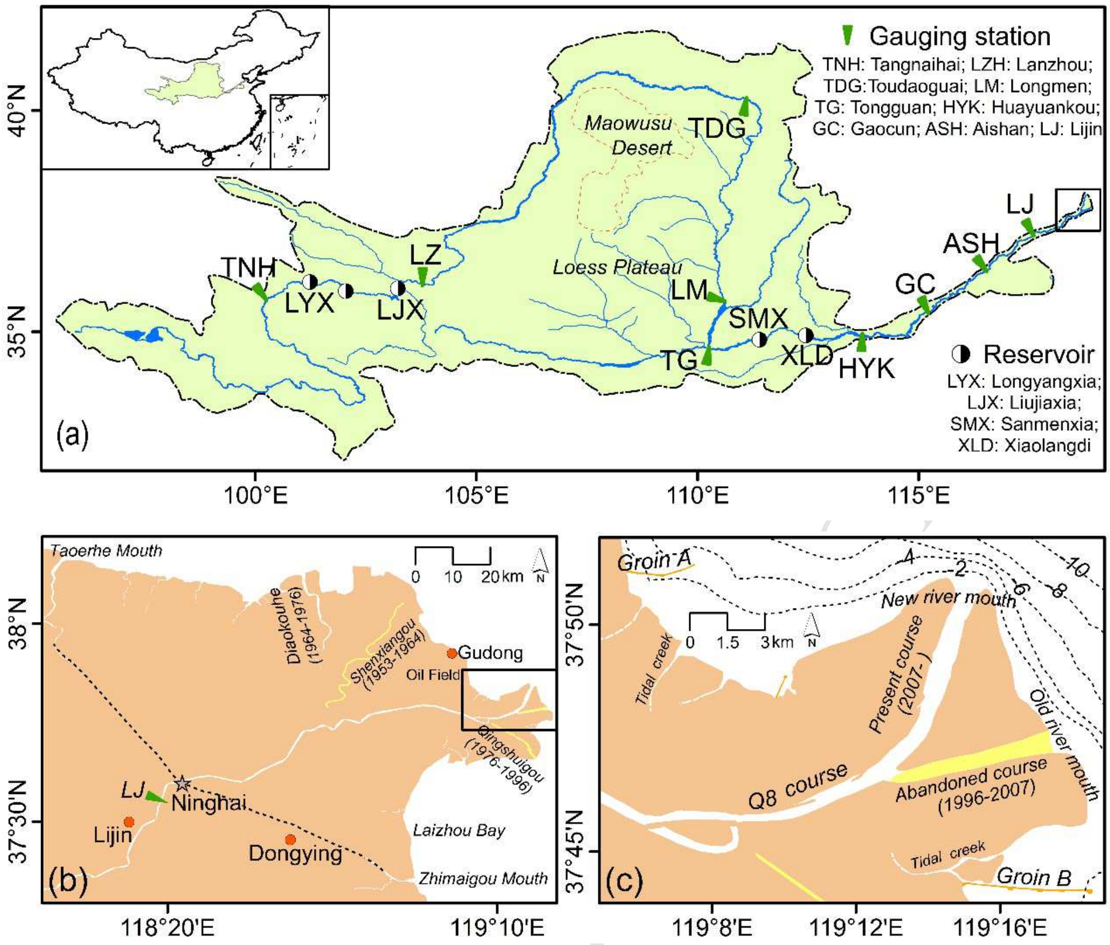

Fig. 1. Study area (a): Yellow River drainage basin, with locations of major gauging stations and reservoirs. (b): range of Yellow River delta, with the historical major channels and the location of fixed channel cross-sections showed by red line. (c): map of the active delta lobe showing the channel change since 1996.

2.2 Variations in river flow to the sea

To measure river flow, we gathered data on annual water discharge (Q) and the sediment load (Qs) of the Yellow River at Lijin (LJ), which was commissioned by the Yellow River Water Conservancy Commission and the River Sediment Bulletin of China. There was a gradual decrease of annual terrestrial sediment transported to the sea during 1950-2012 (Yu et al, 2013). This trend became particularly pronounced after the construction of the Liujiaxia (LJX) reservoir in 1968 (Wang et al, 2017). Each reservoir resulted in a sharp decrease in water and sediment discharges to the sea, reflecting the effects of water storage and sediment sequestration. Values for the period of 1950-1959 before the construction of Sanmenxia (SMX) reservoir can represent the natural conditions of the river basin. The average water discharge and sediment load over this period was 316×10^8 m^3/yr and 7.68×10^8 t/yr (Peng et al, 2010a). By comparison, the water discharge in 2002-2015 fell to 37% of that under natural conditions, and the sediment load accounted for only 11% of the natural flow.

The WSMS has become a human-made ‘‘high-water period’’ for the lower Yellow River and played a dominant role in river input. Although the sediment regulations during 2002-2010 averaged only approximately 20 days per year, they produced 27.6% and 48.9% of the annual water and sediment discharge to the sea, respectively (Yu et al, 2013). Significant amounts of water and sediment were let into the sea only at specific times; therefore, their seasonal characteristics have been noticeably changed under the influence of the WSRS.

3. Data and methods

3.1 Landsat imagery and data measurements

We downloaded all available Landsat TM (Thematic Mapper), ETM+ (Enhanced Thematic Mapper Plus) and OLI (Operational Land Image) data images (path 121 row 34) from 2002 to 2015 when cloud cover was approximately 30 % according to The United States Geological Survey Center for Earth Resources Observation and Science (USGS/EROS). We obtained a total of 285 standard Level 1 Terrain-corrected (L1T) products for this study. We were able to correct the systematic geometric errors of the L1T products using ground control points and a digital elevation model (DEM) to a geolocation accuracy of better than 0.4 pixels. In order to further reduce the geometric errors resulting from waterline distortion, we used the original geolocation of Landsat8-OLI image on June 2nd, 2011 as the benchmark. We then geo-referenced the other images to the fiducial geolocation using the image-to-image module. The at-sensor radiance (digital number, DN) was converted to surface reflectance to reduce the atmospheric effects, which was achieved with the Landsat Ecosystem Disturbance Adaptive Processing System (LEDAPS) atmosphere correction tool (Masek et al., 2006; Vermote et al., 1997).

The hydrodynamic data used in this study included tidal levels, speed and direction of winds, which we sampled hourly during 2004-2016 at a fixed station located at Gudong in the Yellow River delta, shown in Figure 1b. In addition, on June 3rd, 2011, the locations of high tide lines at 81 fixed, equally-spaced cross-sections along the active delta coast were measured by the Institute of the Yellow River Estuarine and Coastal Research (Figure 2a).

3.2 Shoreline Indicators

Due to the dynamic nature of shoreline boundaries, we used these fixed indicators to mark the 'true' shoreline position, the high water line (HWL) which is the preferred indicator for imagery interpretation and easy field location (Pajak and Leatherman, 2002). Most of the traditional HWL techniques rely on aerial photography (Stockdonf and Holman. 2002). Since the remnant surface water of mudflats can remain for extended periods of time (Ryu et al., 2002), the wet-dry line could be interpreted as the HWL (Boak and Turner, 2005). However, these lines do not indicate elevation information, which is crucial for determining temporal shoreline changes. In contrast, a tidal data-based shoreline indicator can be determined by the intersection of the coastal profile with a specific vertical elevation. The waterline is defined as the boundary between a body of water and an exposed land mass in a remotely sensed image. Assuming the waterline is a boundary of equal elevation, one can generate an intertidal Digital Elevation Model (DEM) by comparing a series of waterlines observed under various tidal conditions (Ryu et al., 2002; Zhao et al., 2008).

In this study, isolating waterlines which indicate the instantaneous land-water boundary was the first step. Then, we assigned an elevation to each point on these waterlines using the measured tidal level at Gudong station. The third step was to develop a technique for terrain correction to determine the tidal data-based shoreline position. Finally, we mapped the shoreline time series in order to estimate retreat and advance of the tides.

3.3 Waterline extraction

To observe waterline with the imaging systems, various water indices have been designed to enhance the spectral difference between water and other land cover types. (Lee et al., 2001; Ryu et al., 2002; Xu, 2006).In this study, we adopted a widely accepted water index, the Normalized Difference Water Index (NDWI). This method provides greater accuracy (Mcfeeters, 1996) and has been applied successfully to extract waterline data in highly turbid coastal areas, such as the tidal flats of Bohai Rim (Liu et al., 2016), the tidal flats along the Jiangsu coast in China (Liu et al., 2013), and other intertidal regions across East Asia (Murray et al., 2012). The formulation of NDWI is expressed in the equation below:

$$NDWI = \frac{Green - NIR}{Green + NIR} \tag{1}$$

where Green and NIR represent the green light band and near-infrared band, respectively that correspond to the second and fourth bands of Landsat TM/ETM+ imagery, or the third and fifth bands of the Landsat OLI imagery. We chose a threshold value based on the algorithm suggested by Otsu (1979) to generate binary images (land-water) from the NDWI images. Application of the dilation and erosion operator of mathematical morphology can close the gap of channels at the boundary of binary images, resulting in a generated continuous waterline (Geleynse et al., 2012).

3.4 Tidal-level calibration, intertidal slope and shoreline model

We were able to establish a linear regression model between water level and shoreline position based on the tidal-level calibration and two locations of the waterline. Initially, we extracted two waterlines, l_1 and l_2, from two sets of Landsat satellite images (Table 1) with the shorter interval (8 or 16 days) using the method described in Section 3.3. The two waterlines obtained from these two images at different tidal stages were designated as h_1 and h_2, which were referenced against the tidal data at the Gudong station records.

Although transects generated using the DSAS approach are widely used to calibrate tidal levels of the waterline (Brooks and Spencer, 2010), this technique does have some limitations when it is utilized for defining sinuous waterlines. In this area, the cuspate formation precludes the creation of the necessary transects to calculate shoreline movement. According to Li et al. (2010 & 2014) the orthogonal-transect method assumes that the direction of shoreline change is different at any point. Orthogonal transects are generated at varying angles to ensure the orthogonal to the shorelines at an arbitrary point in time. In this way, researchers are able to capture more realistic shoreline movement and create a more precise, complex, non-straight shoreline change model. Therefore, we constructed orthogonal transects along the gradient direction to more accurately estimate the shore slope.

Each transect was set as orthogonal to the waterlines, and the length of orthogonal transect between these two waterlines, $l_1 - l_2$, represented the distance between waterline positions. We assumed that this intertidal zone had an approximately uniform slope, *p*, defined in Equation (2). Thus, the waterlines were shifted to the tidal data-based shoreline position, *h* using equiangular triangle theory. The shifted distance, *l*, was obtained via Equation 3, shown below:

$$p = \frac{h_1 - h_2}{l_1 - l_2} \tag{2}$$

$$l = \frac{h - h_1}{p} = \frac{(h - h_1)(l_1 - l_2)}{(h_1 - h_2)} \tag{3}$$

Two waterlines with a time interval of no more than 16 days can be composed of 43 pairs among the 285 Landsat images. Considering that the true shoreline shifts rapidly and that 43 pairs of waterlines maybe occupying large space, we constructed

42 groups of orthogonal transects each of which covered two pairs of waterlines that were selected from four adjacent Landsat images. Thus, each orthogonal transect of each group could be used to obtain two intertidal slopes. By examining the differences between those two slopes, we were able to confirm the slope stability. After that, we selected the appropriate slope, shifted the 285 waterlines to determine the shoreline position, namely the average water level in the region from 2004-2016, and completed the shoreline time series mapping.

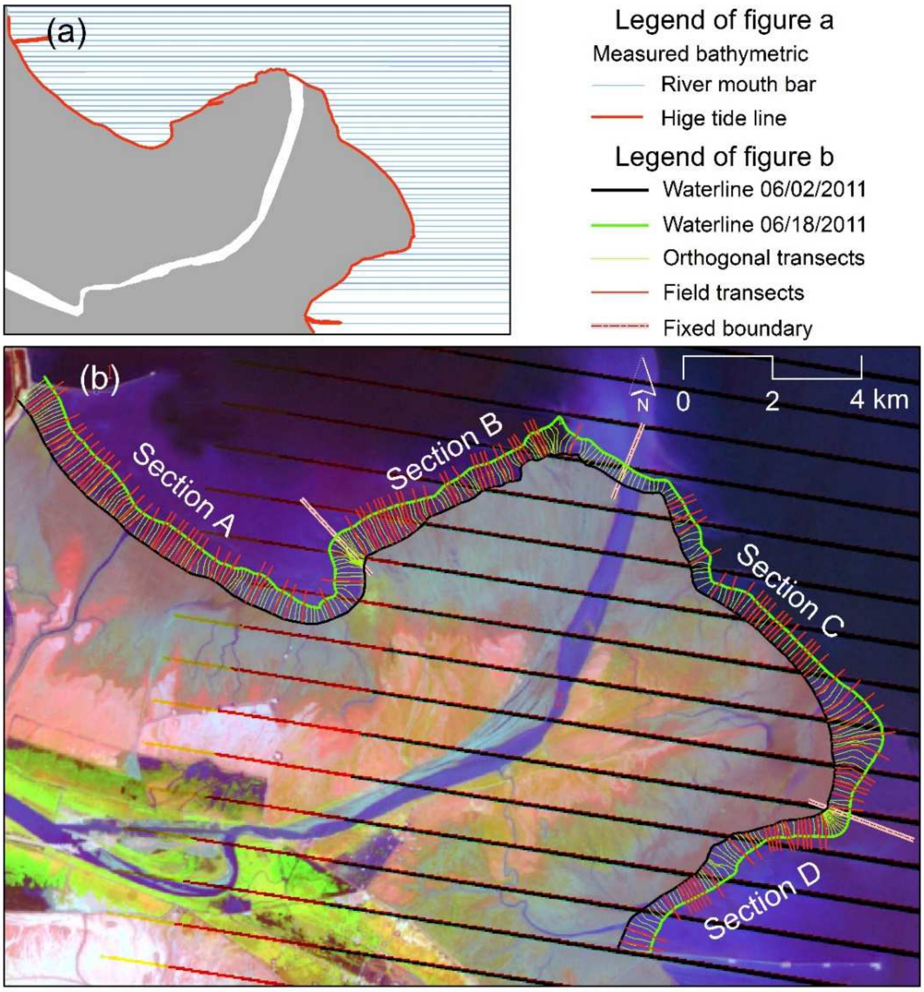

Fig. 2. The distribution of field transects and orthogonal transects. (a) The locations of 81 fixed, equally-spaced cross-sections and high tidal line for boundary measured along the active delta coast (b): The intertidal in June, 2011 divided into A, B, C and D four sections by three fixed boundary. The orthogonal transects and 119 field transects were also shown in (b). Bands of 4, 5

and 3 from Landsat 7 ETM+, acquired on June 2nd, 2011, combine the base map.

Table 1 Summary of the satellite data for tidal-level calibration and intertidal slope calculation of AYRD in 2002-2015. The spatial resolution of those images is 30 m.

Time	2 sets of Landsat -TM-ETM+-OLI satellite images							
series	Date	Time	Sensor	tidal level (cm)	Date	Time	Sensor	tidal level (cm)
1	17/02/2005	10:28:19	TM	42.15	25/02/2005	10:31:23	ETM+	-3.26
2	14/04/2005	10:31:18	ETM+	24.85	22/04/2005	10:28:53	TM	-17.25
3	01/06/2005	10:31:16	ETM+	26.23	17/06/2005	10:31:10	ETM+	-18.50
4	12/08/2005	10:29:45	TM	17.81	20/08/2005	10:31:01	ETM+	-56.24
5	23/10/2005	10:30:57	ETM+	49.27	31/10/2005	10:29:46	TM	-11.52
6	03/05/2006	10:31:46	ETM+	-9.02	19/05/2006	10:31:40	ETM+	52.69
7	04/06/2006	10:31:46	ETM+	-21.36	12/06/2006	10:34:15	TM	-51.52
8	16/09/2006	10:35:31	TM	-26.64	24/09/2006	10:31:12	ETM+	31.15
9	26/10/2006	10:31:23	ETM+	41.85	03/11/2006	10:34:21	TM	1.58
10	11/03/2007	10:30:54	TM	-90.82	27/03/2007	10:32:14	TM	48.28
11	28/04/2007	10:36:24	TM	-10.52	14/05/2007	10:36:15	TM	33.12
12	07/06/2007	10:31:59	ETM+	11.71	15/06/2007	10:35:47	TM	-29.36
13	03/09/2007	10:31:69	TM	46.85	11/09/2007	10:31:33	ETM+	1.65
14	05/03/2008	10:31:54	ETM+	19.21	14/04/2008	10:31:03	TM	-9.02
15	16/05/2008	10:30:27	TM	5.32	24/05/2008	10:31:39	ETM+	-28.69
16	20/08/2008	10:31:17	TM	5.65	28/08/2008	10:30:47	ETM+	-24.73
17	05/09/2008	10:27:18	TM	43.73	13/09/2008	10:32:31	ETM+	-2.36
18	15/10/2008	10:30:24	ETM+	29.23	23/10/2008	10:25:47	TM	-1. 32
19	19/05/2009	10:29:47	TM	6.32	04/06/2009	10:30:03	TM	-10.56
20	07/08/2009	10:30:55	TM	5.21	31/08/2009	10:31:54	ETM+	-24.51
21	03/11/2009	10:32:24	ETM+	-78.16	19/11/2009	10:32:37	ETM+	41.23
22	07/06/2010	10:32:37	TM	-24.81	15/06/2010	10:34:05	ETM+	44.85
23	11/09/2010	10:31:57	TM	-5.25	27/09/2010	10:31:51	TM	41.62
24	06/11/2010	10:34:46	ETM+	46.67	22/11/2010	10:34:32	ETM+	16.21
25	30/03/2011	10:35:20	ETM+	-9.13	15/04/2011	10:35:20	ETM+	53.26
26	02/06/2011	10:35:20	ETM+	-47.68	18/06/2011	10:35:18	ETM+	19.81
27	06/09/2011	10:35:03	ETM+	11.23	22/09/2011	10:34:59	ETM+	-12.75
28	09/11/2011	10:35:13	ETM+	25.41	25/11/2011	10:35:25	ETM+	68.48
29	11/04/2012	10:35:50	ETM+	-37.24	17/04/2012	10:35:47	ETM+	9.57
30	07/08/2012	10:36:46	ETM+	41.62	23/08/2012	10:36:56	ETM+	7.92
31	11/11/2012	10:37:21	ETM+	33.98	27/11/2012	10:37:43	ETM+	-13.15
32	15/02/2013	10:37:55	ETM+	23.45	03/03/2013	10:37:52	ETM+	-13.48
33	10/08/2013	10:36:56	ETM+	-41.85	26/08/2013	10:37:07	ETM+	21.74
34	06/11/2013	10:43:26	OLI	31.57	14/11/2013	10:42:52	ETM+	-12.63
35	06/03/2014	10:38:31	ETM	15.23	14/03/2014	10:42:12	OLI	-25.31
36	01/05/2014	10:41:25	OLI	-12.36	09/05/2014	10:38:59	ETM+	14.75
37	20/07/2014	10:41:33	OLI	34.36	28/07/2014	10:39:20	ETM+	-1.36
38	21/08/2014	10:41:46	OLI	26.60	29/08/2014	10:40:36	ETM+	-5.31
39	16/10/2014	10:39:43	ETM+	51.02	24/10/2014	10:41:54	OLI	-12.36
40	05/02/2015	10:40:25	ETM+	13.56	13/02/2015	10:41:30	OLI	-10.48
41	12/05/2015	10:40:41	ETM+	40.71	20/05/2015	10:40:44	OLI	-19.65

42	08/08/2015	10:41:19	OLI	39.27	16/08/2015	10:40:25	ETM+	-3.84
43	11/10/2015	10:41:42	OLI	-4.95	27/10/2015	10:41:47	OLI	27.54

3.5 Analysis of shoreline dynamics

In order to detect shoreline changes at different timescales, we calculated the Abrupt Change Value (ACV) of the shoreline time series and the average rates of shoreline change based on a total of 27 orthogonal transects generated at a spacing of 500 m along the shoreline which is closest to the land. Figure 3a shows the imageries being used in this study. Seven consecutive imageries made up a group, and we divided the 285 imageries into 273 groups cumulatively. We calculated the time span of each groups and found these 273 time spans were mainly belong to 96-120 d, accounting for 82% (Figure 3b). Thus, detecting an abrupt change of the middle one among seven consecutive shorelines ensured that we calculated the shoreline changes within a similar time interval. The ACV equation (Equation 4) is shown below:

$$C_i = \frac{\sum_{j=i+1}^{j=i+3} y_j - \sum_{j=i-3}^{j=i-1} y_j}{3} \qquad (4)$$

Where y_j indicates the position of the *j*th shoreline and C_i is the *i*th ACV. A positive value represents a seaward abrupt change, and a negative value represents a landward one. Using the shorelines ACV of 27 orthogonal transects as our statistical data, we analyzed the spatial differences of shoreline changes using the *K*-means clustering algorithm based on datasets according to a particular clustering number. We utilized this algorithm to determine the rough number of results and obtain an initial cluster. Then, we used the iterative relocation to improve the *K*-means clustering.

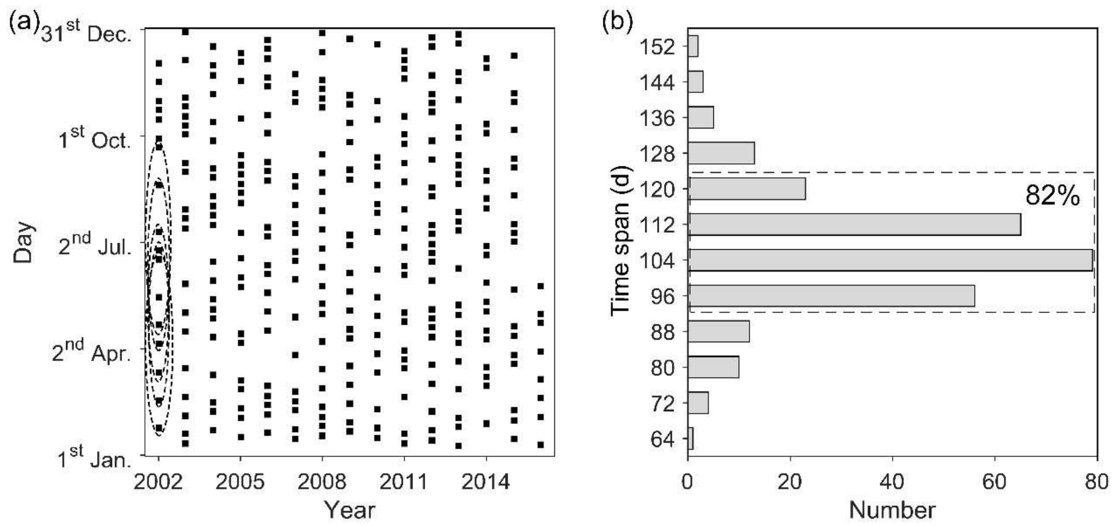

Fig.3. A time table of 285 Landsat imageries. (a) The black dots showed the date of these imageries. Seven consecutive imageries made up a group. These imageries were cumulatively divided 273 groups. The dotted lines circled the first five groups. (b) Frequency distribution of 273 time spans. The time spans belong to 96-120 d accounted for 82%.

The average rates of shoreline change (ARSC) were calculated using the following method (Equation (5)). Initially, we determined this rate between each consecutive pair of time points by calculating the End Point Rate (EPR) method along the orthogonal transects. We were then able to determine the mean rates by averaging the EPRs along each transect:

$$C_r = \sum_{i=1}^{n-1} [(y_{i+1} - y_i)/(t_{i+1} - t_i)] / (n-1) \quad (5)$$

Where y_i represents the position of the ith shoreline at time t_i and n is the number of shorelines.

To test the relationship between the spatiotemporal dynamics of AYRD's shoreline change and the river flow, we examined the correlation between ACV and the river flow at various scales. To determine the effect of marine dynamics on coastal erosion and accretion, we established a Relative Exposure Index (REI) using a Wave

Exposure Model (WEMo). The WEMo is an ArcGIS tool developed by the National Oceanic and Atmospheric Administration (NOAA), and has been used to measure wave exposure in submerged aquatic vegetation (Fonseca et al., 2002) and for shoreline change research (Cowart and Corbett, 2015; Cowart et al., 2011). This numerical model calculates an REI based on hourly wind speed and direction, fetch and bathymetry data to evaluate the extent to which a site is exposed to wind-generated waves in comparison to other sites. In WEMo, fetch is determined by radiating 32 lines at 11.25° angle increments from the point of interest. The fetch lines are then clipped to the area occupied by the bathymetric dataset to obtain the fetch length. To create a single representative metric of fetch, we averaged the 32 fetch lengths to obtain the "mean fetch" value at each shoreline point. Bathymetry and wind data were used to calculate the REI of shoreline in 2011, a unitless value representing wave energy.

4. Results

4.1 Intertidal slope validation and stability

To verify the accuracy of the slope value that was estimated by the above-mentioned method, we compared the calculated gradients with the observed gradients. We obtained the latter from measured bathymetry for the cross sections and high tidal line in June, 2011. Based on the coastal morphology and the distribution of groins, we divided the intertidal data from the active delta into four sections A, B, C and D by establishing three fixed boundaries (Figure 2b). The calculated average gradients of the four sections were 0.688‰, 0.757‰, 0.883‰ and 0.882‰, and were calculated from 109, 79, 87 and 65 orthogonal transects, respectively (Table 2). Connecting the two sounding points cover by the same orthogonal transect constructed the field transect. A total of 119 field transects were obtained, including 34, 28, 33 and 24 in Section A, B, C and D, respectively. The observed gradient values of 0.670‰, 0.743‰, 0.837‰ and 1.018‰, as shown in Table 2, were determined from the ratio of the water depth to the horizontal distance (Table 2). These values were close to the calculated average values, except for Section D because its field transects were unevenly distributed (Figure 2b). Comparisons of each gradient derived from both the 119 field transects and orthogonal transects showed (Figure 4a) that the calculated results conformed well to the observed ones. The Root Mean Square Error (RMSE*v*), between the observed gradients and the calculated ones for the 119 field transects measured in the four sections ranged from 0.024 ‰ to 0.041‰.

We also calculated the root mean square error ($RMSE_s$) for the two intertidal gradients extracted from the same orthogonal transect group. We found that the wind conditions affected the intertidal bed-level (Shi et al, 2017; Zhu et al, 2017). To verify the stability of the slope, we analyzed the relationship among the $RMSE_{s,}$ the offshore wind index (the product of wind speed and frequency), and the sediment load. According to the coastal range and morphology, the southwest wind (including SW, W, S), southeast wind (including SE, E, S), southwest wind (including SW, W, S) and northwest (including NW, N, W) were offshore winds of Sections A, B, C and D, respectively. Figure 4b illustrates an exponential relationship between the $RMSE_s$ and the offshore wind index, where R^2 ranged from 0.8014 to 0.8993 for four sections. There was a weak correlation between the $RMSE_s$ and the sediment load, which suggests that offshore wind is not the governing factors for intertidal slope change. The estimation method also impacted the difference between the two gradients extracted from two pairs of waterlines. When the $RMSE_s$ is less than $RMSE_v$, the difference between the two gradients caused by the remote sensing simulation method. When the $RMSE_s$ equals the $RMSE_v$ (Table 2) of each section, offshore wind index is about 2.4 m/s (Figure 4b). This indicates that the slope of AYRD's intertidal zone is very stable, since the offshore wind index is rarely more than 2.4 m/s. Thus, each waterline could be shifted to the shoreline position with an approximation gradient.

Table 2. Summary of the intertidal gradients derived from both the field transects and the orthogonal transects of four sections.

Sections	Observed intertidal gradient				Calculated intertidal gradient				$RMSE_v$ (‰)
	Transect Quantity	Average gradient(‰)	Maximum gradient(‰)	Minimum gradient(‰)	Transect Quantity	Average gradient(‰)	Maximum gradient(‰)	Minimum gradient(‰)	
A	34	0.670	0.976	0.493	109	0.688	1.167	0.472	0.024
B	28	0.743	1.186	0.485	79	0.767	1.168	0.519	0.034
C	33	0.837	1.331	0.217	87	0.883	1.454	0.341	0.040
D	24	1.018	1.496	0.598	65	0.882	1.474	0.559	0.041

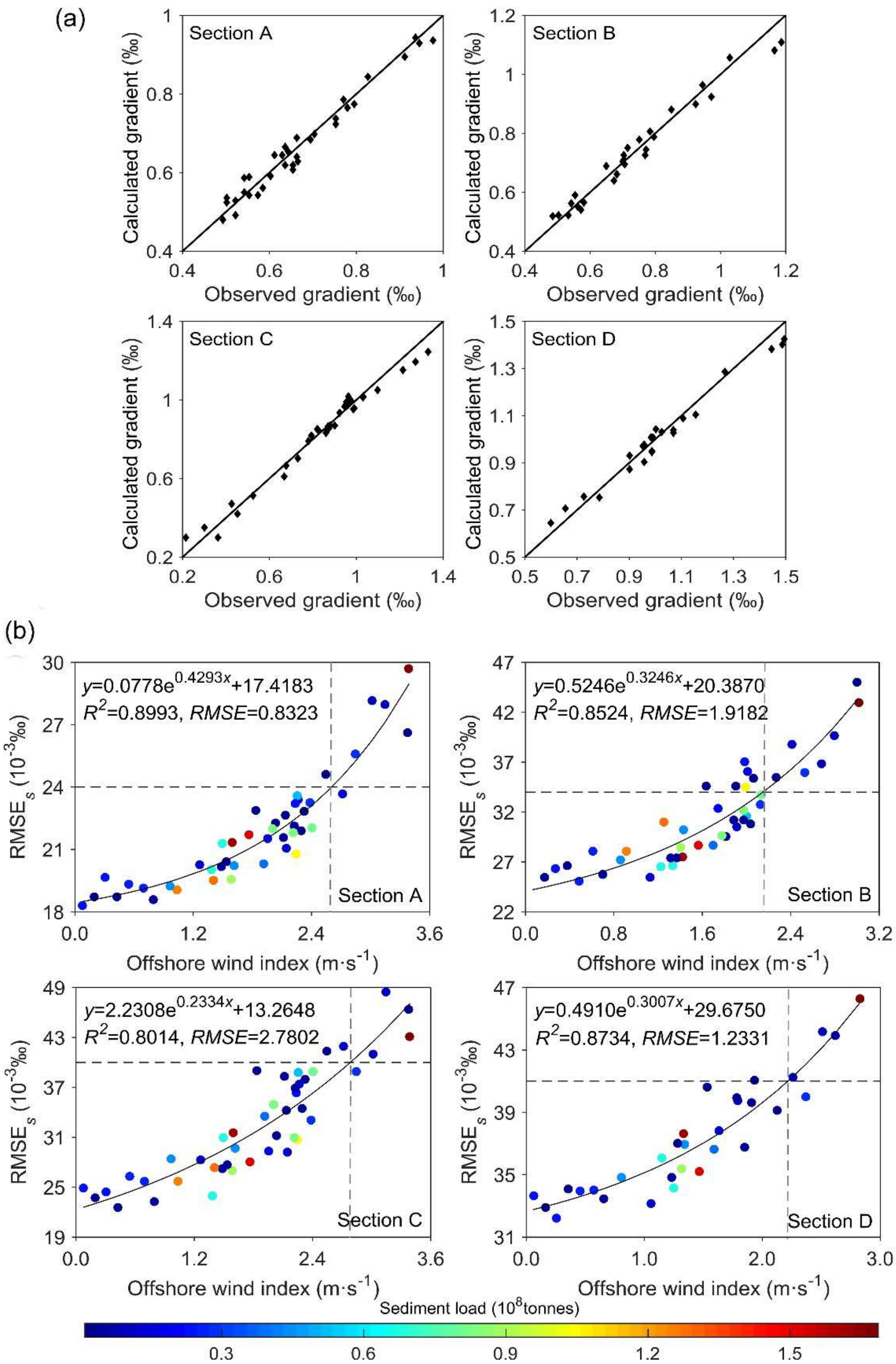

Fig. 4. Intertidal slope validation and stability. (a) Scatter plots of intertidal gradient derived from both the orthogonal transects and the field transects in June, 2011. (b) Scatter plots of $RMSE_s$ for 2 intertidal gradients extracted from the same groups of orthogonal transect. The $RMSE_s$ changes as the offshore wind index and sediment load changes. The color of the point represents the amount of sediment load.

4.2 The spatiotemporal dynamics of shoreline change

Shoreline time series of the active delta from May, 2002 to May, 2016 (Figure 5) indicated an overall seaward trend of the shoreline. Considering the Q8 course shifting toward the northeast in 2007 as the time boundary, the trends can be divided into two categories. Before 2007, overall shoreline shifts were more toward the sea; however, after this point in time, the northeastern shorelines continued their movement toward the sea and the eastern shorelines began to shift toward the land. We divided the 27 transects into eight classes based on the *K*-mean cluster. T1-T8 transects, far from the new mouth of the river on the west side, were the first class. T9 and T10 were the second class, and T11and T12 were the third class, which are located at the east and west sides of the new mouth of the river, respectively. Far from the new mouth of the river on the east side, T13-T18 transects made up the fourth class. T19-T22 transects, located near the old mouth of the river, which is characterized by strong shoreline shifts, can be divided into three classes. T19 and T20 were designated as the fifth class. T21 and T22 were marked as sixth and seventh classes, respectively. T23-T27 transects, including Section D, were the eighth class.

In each class, the shoreline's abrupt changes are essentially the same. Figure 6a shows this phenomenon in the representative transects of the 1-8 classes from 2002 to 2016. Due to the fact that a positive value represents an abrupt seaward change and a negative value represents an abrupt landward change, we were able to obtain a pattern of the spatiotemporal dynamics of shoreline change. The shoreline at the T6-T14 transects mainly moved seaward during 2007 to 2014, while the shoreline at T20-T22 moved to the sea first then to the land. This pattern indicated that Q8's course shift in 2007 had a significant impact on long term annual shoreline changes. Based on the inter-seasonal scale, during 2007-2013, the shoreline at the T6-T14 transects shifted toward the sea during flood season and toward the land during the dry season with the maximum shift occurring as a result the WSRS. The shoreline position at T20-T25 shifted seaward during the flooding season and remained essentially unchanged or moved slightly landward during the dry seasons during the years of 2002-2006. However, during the study period of 2006-2013, there was a distinct landward shift in the drought season and no motion or only a slight seaward shift during the flood season. On the spatial scale, shorelines near the mouth of the river (transects 20-22, before 2007; transects 10-11, after 2007) shifted more significantly than shorelines far from it whether they were landward or seaward. We divided the shoreline of the active delta into two segments: those near the new and old mouths of the river (transects 19-22 and transects 9-12, Figure 5), and those further away from the old and new mouths of the river.

When we analyzed the average rates of shoreline change (ARSC) during the two study periods of 2002-2006 and 2007-2015, (Figure 6b), significant differences between the two segments and both time periods became apparent. The first interval, from 2002 to 2006, was the maximum accretion period of 1.94 km/yr, which accumulated at the nearby mouth of the river (T21).The minimum accretion rate of 0.27 km/yr accumulated at new mouth of the river (T13). The rates declined remarkably during 2007-2015 except for the segment at the nearby mouth of the river

(T10-T13), where the maximum accretion rate was 0.72 km/yr. The old river mouth segment (T19-T22) eroded at a maximum speed of -0.41 km/yr and an average speed of -0.31 km/yr during 2007-2015. Most portions of the coast have grown more slowly than those further away from the segment near the river mouth, and the coast line has gradually become convex in the seaward direction. The average rate of shoreline near the mouth of the river (T19-T22) during 2002-2006 showed a reverse trend of change compared to 2007-2015. During 2007-2015, the area near the new mouth of the river (T10-T13) grew fastest, resulting in shifting of the fan delta apex from east to northeast.

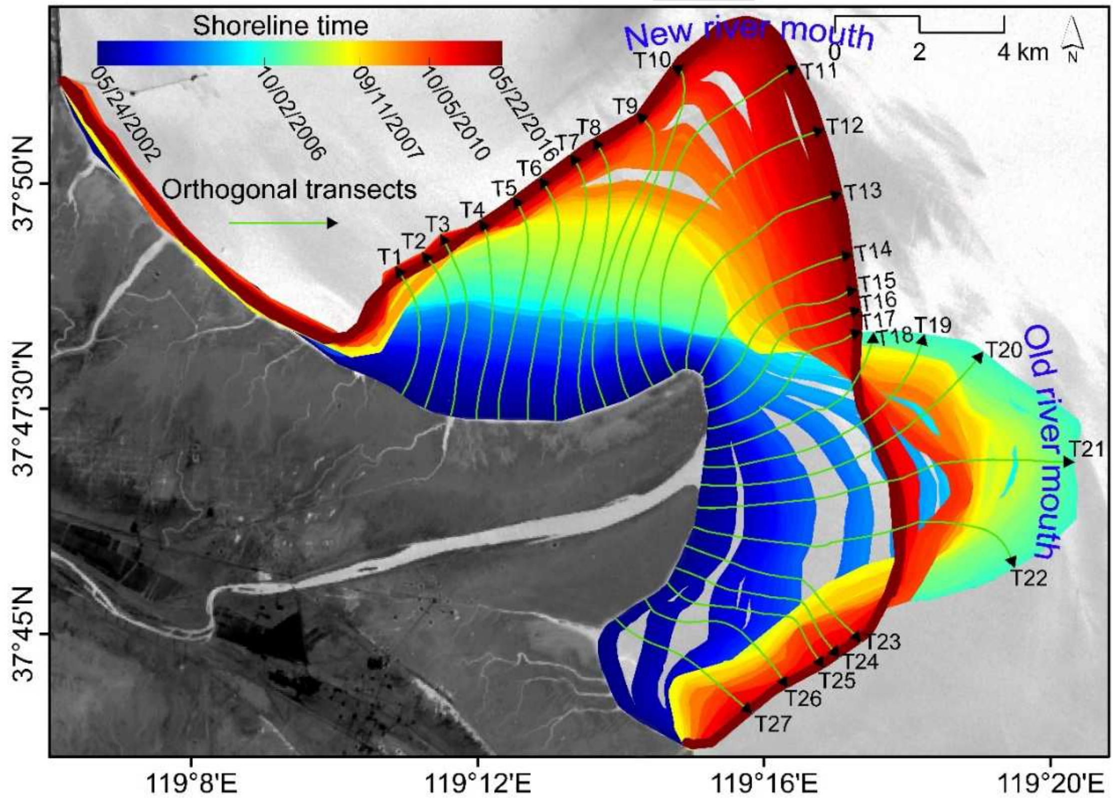

Fig. 5. Shoreline dynamics in active delta from May, 2002 to May, 2016. A total of 27 orthogonal transects were created at 500 m spacing. Landsat 5 TM, acquired on May 24, 2002, combine the base map.

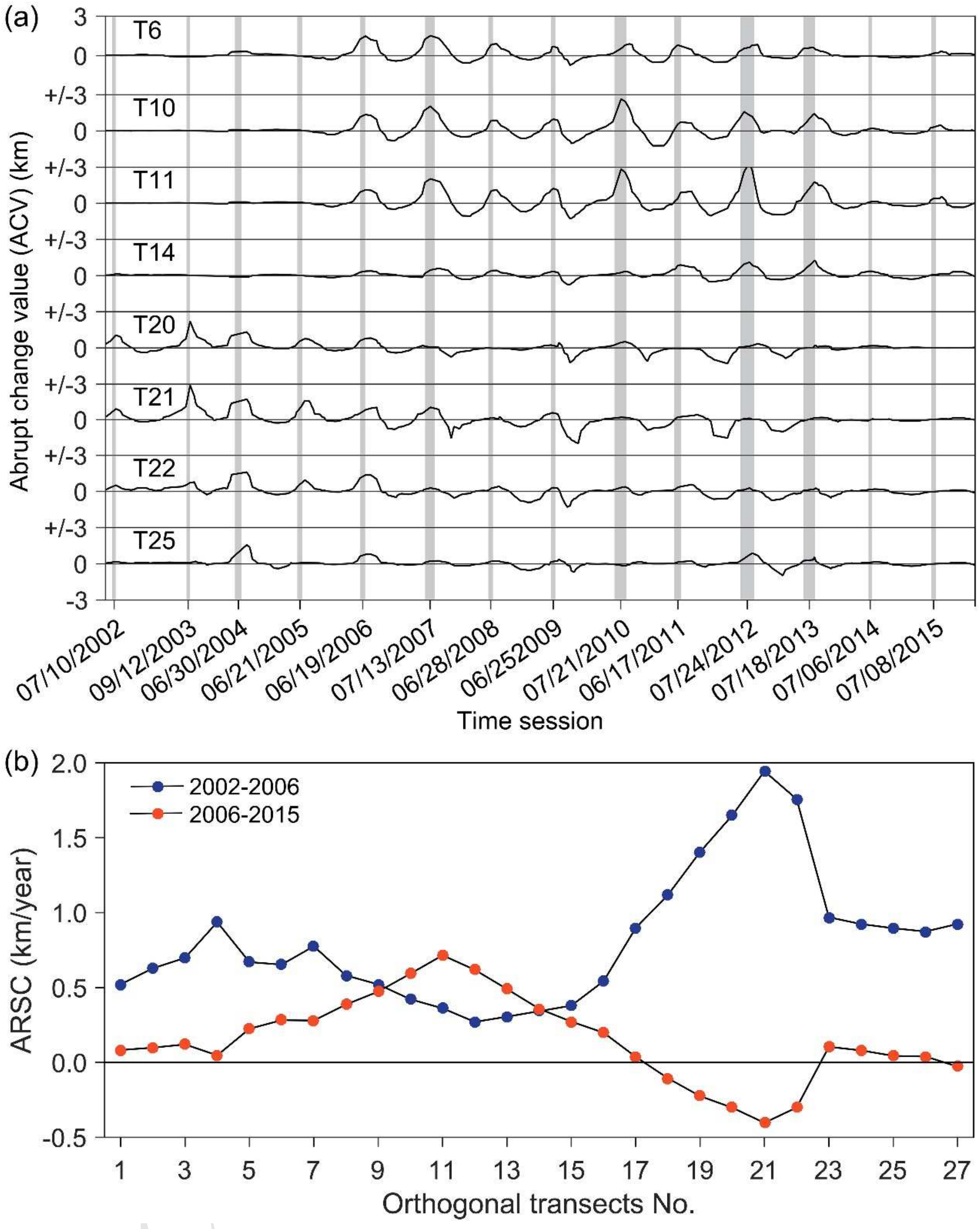

Fig. 6. (a) Shoreline abrupt change in the representative transects of the 1-8 class from 2002 to 2016. Gray sections represent the WSRS period. X-axis is marked by the middle of the annual WSRS. (b) The average rates of shoreline change of two individual periods 2002-2006 and 2007-2015.

4.3 The connection between river flow and wave energy

Table 3 lists the annual flow from the river into the sea, key information about

WSRS regimes and numbers indicating abrupt changes to the shoreline during 2002-2015. We compared the relationship between the average 10% of the largest values of ACV and sediment load (water discharge) after the implementation of the WSRS. (Figure 7a and 7b). We found the correlations to be weak (R^2=0.3016 for the sediment load and R^2=0.4236 for the water discharge) if all transects (ALV_{allt}) are considered. When we focused only on the ALV segments near the mouth of the river (ALV_{rmt}), their correlation became more obvious (R^2=0.7788 for the sediment load and R^2=0.5197 for the water discharge). This fact suggests that transferring large amounts of water and sediment in a highly-efficient model during the WSRS played a significant role in the extension of the sand bar.

Table 3 Annual material to the sea, key information about WSRS regimes and abrupt change value of shoreline during 2002-2015.

Year	Annual sediment load (10^8 t)	Annual water discharge (10^8 m^3)	ACV (m)			WSRS regime		
			The average (ACVa)	ALV of all transects	ALV of river mouth transects	Duration	Sediment load (10^8 t)	Water discharge (10^8 m^3)
2002	0.5424	41.95	120	312	713	Jul.4 ~ Jul. 21	0.664	26.61
2003	3.6894	192.97	164	593	1458	Sep. 6 ~ Sep. 18	1.207	25.91
2004	2.5790	198.89	181	742	1346	Jun. 13 ~ Jul. 19	0.697	47.88
2005	1.9103	206.74	76	457	1045	Jun.15 ~ Jun. 30	0.613	52.44
2006	1.4869	190.34	164	962	993	Jun.15 ~ Jul. 3	0.648	55.44
2007	1.4729	204.21	77	887	1846	Jun.19 ~ Aug. 7	0.973	66.8
2008	0.7723	145.55	34	492	935	Jun.19 ~ Jul. 3	0.598	44.20
2009	0.5617	132.81	-115	574	1053	Jun.19 ~ Jul. 8	0.345	45.62
2010	1.6722	192.97	162	869	2364	Jun.19 ~ Aug. 21	1.644	98.30
2011	0.9273	184.39	-44	503	739	Jun.19 ~ Jul. 12	0.412	53.40
2012	1.8303	282.26	59	914	2132	Jun.19 ~ Aug. 22	1.497	101.06
2013	1.7280	237.07	136	727	1539	Jun.19 ~ Aug. 17	1.388	122.54
2014	0.3007	144.27	-30	157	172	Jun.30 ~ Jul. 12	-	-
2015	0.3137	133.69	-2	236	464	Jun.30 ~ Jul. 17	-	-

The connections among the annual average ACV (ACVa) at 27 of these transects, the annual sediment load (Q_s), and annual water discharge (Q) are presented in

Figures 7c and 7d. There are clear positive trends between an increase in average ACV and runoff or sediment load. The best fit curves are shown in the equations below:

$$ACV_a = 240.08Q_s^{0.34} - 186.96 \quad R^2 = 0.5088, P < 0.005 \tag{6}$$

$$ACV_a = -2.21\text{e}11Q^{-4.26} + 140.35 \quad R^2 = 0.5072, P < 0.005 \tag{7}$$

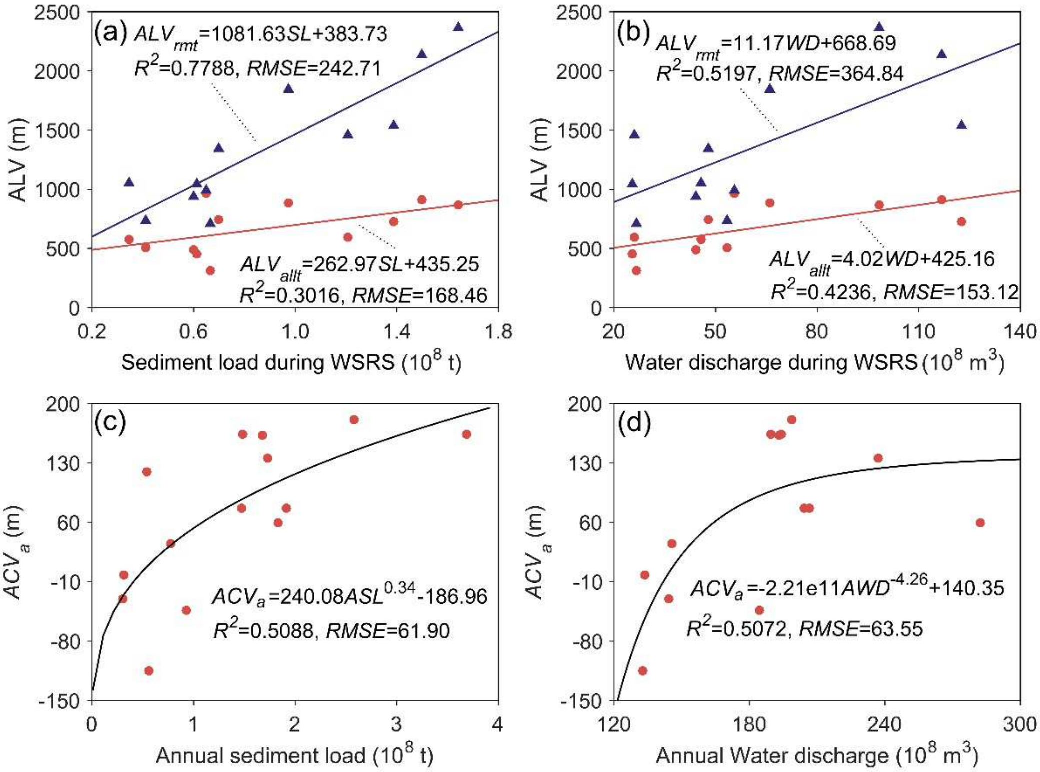

Fig. 7. The annual WSRS influenced the average maximum VAC of each year, especially the nearby river mouth segment. (a) Relations between sediment load and during the WSRS and the average of the 10% largest values (ALV) of shoreline ACV, and (b) represent the water discharge. (c) Relations between annual sediment load and average ACV, and (d) represent the water discharge.

Equation (6) depicts the ACV_a and annual sediment load, and Equation (7) illustrates the ACV_a and annual water discharge. Figure 7c and Equation (6) indicate that the ACV_a increased with sediment load, while the rate of change gradually decreased. When ACV_a is 0, Q_s is 0.48×10^8, this indicates that the critical annual sediment load must be 0.48×10^8 t/yr to maintain the annual balance of the active delta between 2002 and 2015. Figure 7d and Equation (7) show that the ACV_a increases with increasing water discharge. When ACV_a is 0, Q is 144.37×10^8, this indicates that the critical annual water discharge must be 144.37×10^8 m^3/yr to maintain the annual balance of the active delta between 2002 and 2015. However, the ACV_a remains constant at high annual water discharge (about more than 200×10^8 m^3, Figure 7d), which indicates that water discharge is not a persistent control factor for shoreline change.

Wave energy is an essential element of shoreline erosion rates. To represent it, we utilized WEMo to calculate the relative exposure index (REI) in the crossover points of 17 shorelines as well as the transects in 2011 (Figure 8a). The REI values ranged from 137 to 7,967, with an average of 3,742. Over half the shoreline points (53%), with an REI greater than the average (3742), were located a near the mouth of the river.

By applying a linear regression (solid line) between ACV and REI (Figure 8b1), the relationship can be described by the following equation:

$$ACV = -0.0675REI + 313 \quad R^2 = 0.2312, P < 0.001 \tag{8}$$

Figure 8b1 and Equation 8 show that the ACV decreases as REI increases; however, the statistical linear relationship explained little (~20%) of the variation in the data. According to the linear relationship, we calculated the critical REI, 4,637 when ACV was 0, indicating that the nearby mouth of the river segment whose REI was mostly higher than the critical value of 4,637 would be easily eroded. Due to the fact that this result seems to contradict the above analysis, we performed the analysis with another model.

Local weighted regression scatter smoothing (LOWESS), a non-parametric regression model, is a powerful tool for examining the relationship between dimensional variables. The main purpose of LOWESS is to fit the polynomial regression curve into the partial subset data in order to observe the rules and trends of the local data. The result (Figure 8b2), smoothed by LOWESS, implies that the lighter the curve color, the greater the proportion of the data. The white curve is almost linear and the trend to the fitting curve in Figure 8b1, while the black line is more inconsistent. In addition, ACV at two REI ranges, 1,500-3,000 and 4,500-6,000, deviated from the regression curve significantly and had negative and positive deviations, respectively. These two ranges were located mainly in Section D and in the nearby mouth of the river, respectively (Figure 8a). This indicates that the regression curve underestimated the ACV of this segment and overestimated the area of Section D.

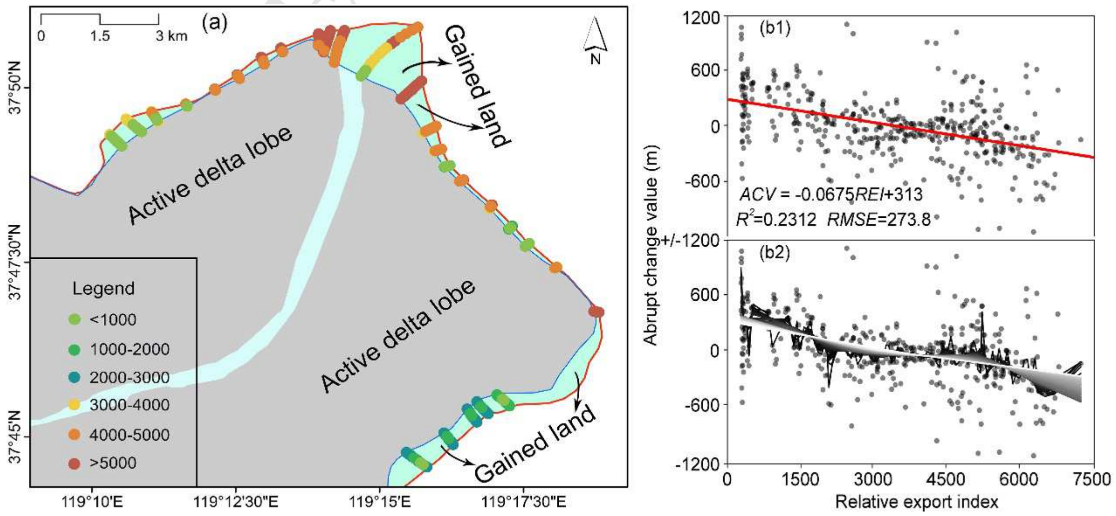

Fig. 8. (a) The relative exposure index (REI) in the crossover point of 17 shorelines and transects

in 2011 calculated by WEMo. The color of the point represents the intensity of the REI. (b1) Linear relationship between shoreline abrupt change value and relative exposure index. A linear regression (red solid line) has been applied. (b2) Curve generated by local weighted regression scatter smoothing (LOWESS), the lighter the curve color the greater the proportion of the data.

5. Discussion

The point-based approach is a conservative method for calculating change on estuarine shorelines (Cowart and Corbett, 2015; Cowart et al., 2011), because it uses the nearest distance between shorelines. However, it must be noted that the orthogonal- transect method could be used to describe the realistic movement along the highly sinuous shoreline.

The AYRD is impacted not only by river flow but also by a series factors, such as coastal processes, structural geology, meteorological conditions, human activity, sea level rise and land subsidence, etc. (Zang, 1996; Tian et al., 1997; Chu et al., 2006; Jiang et al., 2017; Liu et al., 2014a; Liu et al., 2017;). In our study area, although the Q8 was a manually excavated course, the land-use and structural geology did not change significantly over the study period (Cui et al., 2011). Therefore, we concluded that the active delta evolution is controlled by river flow supply and ocean dynamics (natural process) as well as human activities.

The critical sediment load (0.48×10^8 t/yr, during 2002-2015) for the Q8 estuary in this paper accounted for 30% of the value (1.63×10^8 t/yr, during 1996-2005) calculated by Cui, et al. (2011). The reasons for this can be attributed to the following aspects. First, the durations of the targeted times are different. According to Cui, et al. (2011), when the Q8 estuary was in its infancy, it required more sediment load to fill the increasing space for the new submerged delta. Since the implementation of the WSRS, the coefficient of incoming sediments (the ration of suspended sediment concentration and water discharge) in the trail channel has gradually decreased, with an average of 0.011 $kg \cdot s/m^6$ (Wang et al., 2015), which is lower than the critical value of channel erosion (0.014 $kg \cdot s/m^6$, Hu et al., 2005). The riverbed in the lower reaches downstream of LJ has scoured, which increased practical sediment load due to implementation of the WSRS. Third, instead of focusing on annual shoreline intervals, we paid attention to the shoreline on season and event scales. We found that the annual water and sediment discharge was typically uneven for seasonal distribution. This has been exacerbated by the implementation of WSRS, which has caused the different erosion-accretion patterns between the flood and drought season, namely "deposition in flood season and erosion in drought season". Focusing only on annual-scale variability of the shoreline may leave out important shoreline characteristics which may occur seasonally. Moreover, two groins (Figure 1c) that formed off the mouth of the Yellow River after 2005 nourished the coast and protected it from rapid seaward progradation by trapping the sediment that was transported by the currents (Bi et al., 2014).

The Yellow River sediment load during 2002-2015 was approximately 1.4×10^8 t/yr, which kept the active delta in a state of relatively rapid accretion. However, due to the WSRS, the river bed sediments in the lower reaches have become increasingly coarser than ever before (Kong et al., 2015b, Ma et al., 2017) and the river bed is becoming more resistant to erosion. In 2008, riverbed sediment in the lower reaches of the Yellow River was coarser than it had been in 1999. This was particularly true for the HYK and ASH (Figure 1b) reaches in which the median grain size increased from 0.06 mm to 0.21 mm and from 0.04 mm to 0.07 mm, respectively (Yu et al, 2013). As a result, when clear water discharged from upstream during WSRS, the suspended sediment that was concentrated at the gauging stations has been steadily dropping. From 2000 to 2015, the cumulative water discharge and the cumulative sediment load had a clear linear positive correlation. Take the year of 2006 as a time boundary, two linear functions could fit their relationship. The slope of fitting curves decreased after 2006, which indicates that the erosion rate of unit runoff has gradual diminished (Long et al, 2017). This trend caused a decline in the annual sediment load in recent years, especially in 2014 (0.3007×10^8 t) and 2015 (0.3137×10^8 t). This was less than the critical sediment load, which seemly explained the shift of the AYRD's shoreline from a rapid advance to an equilibrium condition.

In addition to the sediment flow, the dynamics of deltaic shorelines is also closely related to the waves and tidal action off the subaerial delta, which accounts for the inherent complexity of the coastal environment (Fagherazzi et al., 2015). Although there has been limited study on AYRD erosion by violent storms and waves, shoreline retrogradation is still a concern because of the shape of the convex coast and less sediment load during drought season. Wu et al. (2015) found that the buoyant river plume was the main cause of the sediment dispersal pattern during the WSRS, and the river sediment discharge to the sea mostly accumulated within a limited coastal area, which effectively extended the subaerial delta. Thus, the observed low correlation between AYRD's shoreline abrupt change value and REI was mainly caused by the rapid deposition of nearby segments at the mouth of the river where the REI was higher after the implementation of WSRS.

6. Conclusion

Our research presents detailed spatiotemporal dynamics of the shoreline's annual-scale, season-scale and event-scale changes of AYRD since the implementation of WSRS. We utilized a scheme based on slope correction and orthogonal-transect method to model the shoreline position. Assessment of the estimated intertidal slopes indicated that these techniques are useful for calculating the slope of complex curving beaches. The RMSE between measured slopes and those estimated was less than that of the survey slopes by approximately one order of magnitude.

Based on the orthogonal transects and the estimated beach slope, we mapped the shoreline time series. The results revealed that the course shift in 2007 on Q8 had a significant impact on shoreline inter annual changes, and the active delta experienced a pattern of "deposition in flood season and erosion in drought season" that coincided with the implementation of the WSRS. The annual WSRS regime plays a dominant role in river flow to the sea and affects the average annual maximum ACV, especially the segment near the mouth of the river. Our results revealed that river flow has had a significant impact on shoreline changes in the active delta, potentially more than wave energy in this environment with rapid deposition of the segment near the mouth of the river during the flood season. In order to maintain the annual balance of the active delta during the period between 2002 and 2015, critical annual runoff and sediment loads must be 0.48×10^{8} t/yr and 144.37×10^{8} m^3/yr. Riverbed scouring during the WSRS has weakened since 2006; therefore, the amount of annual sediment discharged in 2014 and 2015 was less than the critical sediment load. The amount of water released from the XLD dam during the WSRS should be increased to maintain riverbed scouring and stabilize seaward progradation of AYRD. It is our hope that these findings will aid in the management of the AYRD and the lower channel. Engineers should ensure water-sediment regulation or river damming to strike a balance between suspended sediment delivery and delta growth.

Acknowledgements

This study was partly supported by the National Key Research and Development Program of China (No. 2017YFC0405503) and the Open Research Fund (ORF) of SKLEC (SKLEC-KF201503). We would like to thank USGS for providing Landsat imagery. We also would like to thank the Yellow River Water Conservancy Commission of China and Institute of the Yellow River Estuary and Coast Science for the hydrological and bathymetric data.

References

Ali, E.M., and El-Magd, I.A., 2016. Impact of human interventions and coastal processes along the Nile delta coast, Egypt during the past twenty-five years. Egyptian Journal of Aquatic Research 42(1), 1-10.

Anthony, E.J., Brunier, G., Besset, M., Goichot, M., Dussouillez, P., Nguyen, V.L., 2015. Linking rapid erosion of the Mekong river delta to human activities. Scientific Reports 5, 14745.

Berger, A.R., and Iams, W.J., 1996. Geoindicators: Assessing Rapid Environmental Changes in Earth Systems. Rotterdam, 466p.

Blum, M.D., Roberts, H.H., 2009. Drowning of the Mississippi delta due to insufficient sediment supply and global sea-level rise. Nature Geoscience 2(7), 488-491.

Bi, N.S., Wang, H.J., Yang, Z.S., 2014. Recent changes in the erosion-accretion patterns of the active Huanghe (Yellow River) delta lobe caused by human activities. Continental Shelf Research 90, 70-78.

Boak, E.H., Turner, I.L., 2005. Shoreline definition and detection: a review. Journal of Coastal Research 21 (4), 688-703.

Brooks, S. M., Spencer, T., 2010. Temporal and spatial variations in recession rates and sediment release from soft rock cliffs, Suffolk coast, UK. Geomorphology 124(1), 26-41.

Carriquiry, D., Sánchez, A., Camacho-Ibar, V. F., 2001. Sedimentation in the northern Gulf of California after cessation of the Colorado River discharge. Sedimentary Geology 144(1-2), 37-62.

Chen, W.W., Chang, H.K., 2009. Estimation of shoreline position and change from satellite images considering tidal variation. Estuarine, Coastal and Shelf Science 84(1), 54-60.

Choung, Y.J., Jo, M.H., 2016. Shoreline change assessment for various types of coasts using multi-temporal Landsat imagery of the east coast of South Korea. Remote Sensing Letters 7(1), 91-100.

Chu, Z.X., Sun, X.G., Zhai, S.K., Xu, K.H., 2006. Changing pattern of accretion/erosion of the modern Yellow River (Huanghe) subaerial delta, China: based on remote sensing images. Marine Geology 227(1-2), 13-30.

Cowart, L., Corbett, D.R., 2015. Analyzing estuarine shoreline change: a case study of cedar island, North Carolina. Journal of Coastal Research 26(5), 817-830.

Cowart, L., Corbett, D.R., Walsh, J.P., 2011. Shoreline change along sheltered coastlines: insights from the Neuse river estuary, NC, USA. Remote Sensing 3(7), 1516-1534.

Cui, B.L., Li, X.Y., 2011. Coastline change of the Yellow River estuary and its response to the sediment and runoff (1976-2005). Geomorphology 127(1-2), 32-40.

Cui, B., Yang, Q., Yang, Z., Zhang, K., 2009. Evaluating the ecological performance of wetland restoration in the Yellow River Delta, China. Ecological Engineering 35 (7), 1090-1103.

Dar, I.A., Dar, M.A., 2009. Prediction of shoreline recession using geospatial technology: A case study of Chennai Coast, Tamil Nadu, India. Journal of Coastal Research 25 (6), 1276-1286.

Dewi, R., Bijker, W., Stein, A., Marfai, M., 2016. Fuzzy classification for shoreline change monitoring in a part of the northern coastal area of Java, Indonesia. Remote Sensing 8(3), 190.

Dolan, R., Hayden, B.P., May, P., May, S., 1980. The reliability of shoreline change measurements from aerial photographs. Shore and Beach 48(4), 22-29.

Du, J.L., Yang, S.L., Feng, H., 2016. Recent human impacts on the morphological evolution of the Yangtze River delta foreland: a review and new perspectives. Estuarine, Coastal and Shelf Science 181, 160-169.

Ekercin, S., 2007. Coastline change assessment at the Aegean Sea Coasts in Turkey using multitemporal Landsat imagery. Journal of Coastal Research 23, 691-698.

Fonseca, M.S., Robbins, B.D., Whitfield, P.E., Wood, L., Clinton, P., 2002. Evaluating the Effect of Offshore Sandbars on Seagrass Recovery and Restoration in Tampa Bay through

Ecological Forecasting and Hindcasting of Exposure to Waves. St. Petersburg, Florida: Tampa Bay Estuary Program.

Fagherazzi, S., Edmonds, D.A., Nardin, W., Leonardi, N., Canestrelli, A., Falcini, F., Jerolmack, D.J., Mariotti, G., Rowland, J.C., and Slingerland, R.L., 2015. Dynamics of river mouth deposits. Reviews of Geophysics 53(3), 642-672.

Fanos, A.M., 1995. The impact of human activities on the erosion and accretion of the Nile delta coast. Journal of Coastal Research 11(3), 821-833.

Geleynse, N., Voller, V. R., Paola, C., Ganti, V., 2012. Characterization of river delta shorelines. Geophysical Research Letters 39(17), 17402.

Gens, R., 2010. Remote sensing of coastlines: detection, extraction and monitoring. International Journal of Remote Sensing 31(7), 1819-1836.

Gratiot, N., Anthony, E. J., Gardel, A., Gaucherel, C., Proisy, C., Wells, J.T., 2008. Significant contribution of the 18.6 year tidal cycle to regional coastal changes. Nature Geoscience, 1, 169-172.

Hu, C.H., 2005. Variation of water and sediment processes and complex responses of rivers in the Yellow River. Science Press, Beijing, 448p (in Chinese).

Jangir, B., Satyanarayana, A.N.V., Swati, S., Jayaram, C., Chowdary, V.M., Dadhwal, V.K., 2016. Delineation of spatio-temporal changes of shoreline and geomorphological features of Odisha coast of India using remote sensing and GIS techniques. Natural Hazards 82(3), 1437-1455.

Jiang, C., Pan, S.Q., Chen, S.L., 2017. Recent morphological changes of the Yellow River (Huanghe) submerged delta: causes and environmental implications. Geomorphology 293, 93-107.

Jones, B.M., Arp, C.D., Jorgenson, M.T., Hinkel, K.M., Schmutz, J.A., Flint, P.L., 2009. Increase in the rate and uniformity of coastline erosion in arctic Alaska. Geophysical Research Letters 36(3), 151-157.

Karsli, A.F., Guneroglu, A., Dihkan, M., 2011. Spatio-temporal shoreline changes along the southern black sea coastal zone. Journal of Applied Remote Sensing 5(1), 3545.

Khomsin, 2017. Analysis of east Surabaya shoreline determination using tidal data, image satellite and RTK-GNSS. Applied Mechanics and Materials 862, 41-45.

Kong, D., Miao, C., Borthwick, A.G.L., Duan, Q.Y., Liu, H., Sun, Q.H., Ye, A.Z., Di, Z.H., Gong, W., 2015a. Evolution of the Yellow River delta and its relationship with runoff and sediment load from 1983 to 2011. Journal of Hydrology 520, 157-167.

Kong, D., Miao, C., Wu, J., Duan, Q., Sun, Q., Ye, A., Di, Z., Gong, W., 2015b. The hydro-environmental response on the lower Yellow River to the water-sediment regulation scheme. Ecological Engineering 79, 69-79.

Kuenzer, C., Ottinger, M., Liu, G.H., Sun, B., Baumhauer, R., Dech, S., 2014. Earth observation-based coastal zone monitoring of the Yellow River delta: dynamics in China's second largest oil producing region observed over four decades. Applied Geography 55, 92-107.

Lee, K.S., Kim, T.H., Yun, Y.S., Sang, M.S., 2001. Spectral characteristics of shallow turbid water near the shoreline on inter-tidal flat. Korean Journal of Remote Sensing 17 (2): 131-139.

Li, W.Y., Gong, P., 2016. Continuous monitoring of coastline dynamics in western Florida with a 30-year time series of Landsat imagery. Remote Sensing of Environment 179, 196-209.

Li, X., Zhou, Y.X., Kuang, R.Y., 2010. Analysis and trend prediction of shoreline evolution in Chongming Dongtan, Shanghai. Journal Jilin University (Earth Science Edition) 40 (2), 417-424 (in Chinese).

Li, X., Zhou, Y.X., Zhang, L., Kuang, R., 2014. Shoreline change of Chongming Dongtan and response to river sediment load: a remote sensing assessment. Journal of Hydrology 511(4), 432-442.

Liu, F., Chen, H., Cai, H., Luo, X., Ou, S., Yang, Q., 2017. Impacts of ENSO on multi-scale variations in sediment discharge from the Pearl River to the South China Sea. Geomorphology 293.

Liu, F., Yuan, L., Yang, Q., Ou, S., Xie, L., Cui, X., 2014a. Hydrological responses to the combined influence of diverse human activities in the Pearl River delta, China. Catena, 113(1), 41-55.

Liu, F., Yang, Q.S., Chen, S.L., Luo, Z.F., Yuan, F., Wang, R.T., 2014b. Temporal and spatial variability of sediment flux into the sea from the three largest rivers in China. Journal of Asian Earth Sciences 87(12), 102-115.

Liu, X., Gao, Z., Ning, J., Yu, X., Zhang, Y., 2016. An improved method for mapping tidal flats based on remote sensing waterlines: a case study in the Bohai Rim, China. IEEE Journal of Selected Topics in Applied Earth Observations and Remote Sensing 9(11), 5123-5129.

Liu, Y., Li, M., Mao, L., Cheng, L., Chen, K., 2013. Seasonal pattern of tidal-flat topography along the Jiangsu middle coast, China, using HJ-1 optical images. Wetlands 33(5), 871-886.

Long, Y., Wang, H.J., Bi, N.S., Zhang, Y., Wu, X., 2017. Evolution of active Yellow River (Huanghe) delta under the Water and Sediment Regulation Scheme (WSRS). Marine

Geology Frontiers 33(3): 8-11 (in Chinese).

Ma, H., Nittrouer, J.A., Naito, K., Fu, X., Zhang, Y., Moodie, A. J., Wang, Y., Wu, B. Parker, G., 2017. The exceptional sediment load of fine-grained dispersal systems: Example of the Yellow River, China. Science Advances, 3(5), e1603114.

Maiti, S., Bhattacharya, A.K., 2009. Shoreline change analysis and its application to prediction: a remote sensing and statistics based approach. Marine Geology 257(1), 11-23.

Masek, J.G., Vermote, E.F., Saleous, N.E., Wolfe, R., Hall, F.G., Huemmrich, K.F., Gao, F., Kutler, J., Lim, T.K., 2006. A Landsat surface reflectance dataset for North America, 1990-2000. IEEE Geoscience and Remote Sensing Letters 3, 68-72.

Mcfeeters, S.K., 1996. The use of the normalized difference water index (NDWI) in the delineation of open water features. International Journal of Remote Sensing 17(7), 1425-1432.

Milliman, J.D., 1997. Blessed dams or damned dams? Nature 388, 325-326.

Morton, R.A., 1998. Evaluation of shorelines and legal boundaries controlled by water levels on sandy beaches. Journal of Coastal Research 14(4), 1373-1384.

Murray, N.J., Clemens, R.S., Phinn, S.R., Possingham, H.P., Fuller, R.A., 2014. Tracking the rapid loss of tidal wetlands in the Yellow Sea. Frontiers in Ecology and the Environment 12, 267-272.

Mujabar, P.S., Chandrasekar, N., 2013. Shoreline change analysis along the coast between Kanyakumari and Tuticorin of India using remote sensing and GIS. Arabian Journal of Geosciences 6(3), 647-664.

Murray, N.J., Phinn, S.R., Clemens, R.S., Roelfsema, C.M., Fuller, R.A., 2012. Continental scale mapping of tidal flats across East Asia using the Landsat archive. Remote Sensing 4(11), 3417-3426.

Otsu, N., 1979. Threshold selection method from gray-level histograms. IEEE Transactions on Systems, Man and Cybernetics 9(1), 62-66.

Ottinger, M., Kuenzer, C., Liu, G., Wang, S., Dech, S., 2013. Monitoring land cover dynamics in the Yellow River delta from 1995 to 2010 based on Landsat-5 TM. Applied Geography 44(4), 53-68.

Pajak, M.J., Leatherman, S., 2002. The high water line as shoreline indicator. Journal of Coastal Research 18(2), 329-337.

Pardo-Pascual, J.E., Almonacid-Caballer, J., Ruiz, L.A., Palomar-Vázquez, J., 2012. Automatic extraction of shorelines from Landsat TM and ETM+ multi-temporal images with subpixel precision. Remote Sensing of Environment 123, 1-11.

Peng, J., Chen, S.L., 2010a. Response of delta sedimentary system to variation of water and sediment in the yellow river over past six decades. Journal of Geographical Sciences 20(4), 613-627.

Peng, J., Chen, S.L., Dong, P., 2010b. Temporal variation of sediment load in the Yellow River basin, China, and its impacts on the lower reaches and the river delta. Catena 83(2-3), 135-147.

Phillips, J.D., 1986. Spatial analysis of shoreline erosion, Delaware Bay, New Jersey. Annals of the Association of American Geographers 76(1), 50-62.

Rahman, A.F., Dragoni, D., El-Masri, B., 2011. Response of the Sundarbans coastline to sea level rise and decreased sediment flow: A remote sensing assessment. Remote Sensing of

Environment 115, 3121-3128.

Rao, K.N., Subraelu, P., Kumar, K.C.V.N., Demudu, G., Malini, B.H., Rajawat, A.S., 2010. Impacts of sediment retention by dams on delta shoreline recession: evidences from the Krishna and Godavari deltas, India. Earth Surface Processes and Landforms 35(7), 817-827.

Rao, P.P., Nair, M.M., Raju, D.V., 1985. Assessment of the role of remote sensing techniques in monitoring shoreline changes: a case study of the Kerala coast. International Journal of Remote Sensing 6(3-4), 549-558.

Ryu, J.H., Won, J.S., Min, K.D., 2002. Waterline extraction from Landsat TM data in a tidal flat: A case study in Gomso Bay, Korea. Remote Sensing of Environment 83, 442-456.

Sánchez-Arcilla, A., Valdemoro, H.I., 1998. The Ebro delta: morphodynamics and vulnerability. Journal of Coastal Research 14(3), 754-772.

Shaw, J.B., Wolinsky, M.A., Paola, C., Voller, V.R., 2008. An image-based method for shoreline mapping on complex coasts. Geophysical Research Letters 35(12), 150-152.

Shi, B.W., Yang, S.L., Wang, Y.P., Li, G.C., Li, M.L., Li, P., Li, C., 2017. Role of wind in erosion-accretion cycles on an estuarine mudflat. Journal of Geophysical Research: Oceans 122, 193-206.

Song, C.C., Sun, X.J., Wang, J., Li, M.Y., Zheng, L., 2015. Spatio-temporal characteristics and causes of changes in erosion-accretion in the Yangtze (Changjiang) submerged delta from 1982 to 2010. Journal of Geographical Sciences 25(8), 899-916.

Stockdonf, H.F., Holman, R.A., 2002. Estimation of shoreline position and change using airborne topographic Lidar data. Journal of Coastal Research 18(3), 502-513.

Sui, X., Chen, L., Chen, A., Wang, D.S., Wang, W.L., Ge, H.F., Ji, G.D., 2015. Assessment of temporal and spatial landscape and avifauna changes in the Yellow River wetland natural reserves in 1990-2013, China. Ecological Engineering 84(3), 520-531.

Syvitski, J.P.M., Kettner, A.J., Overeem, I., Hutton, E.W.H., Hannon, M.T., Brakenridge, G.R., Day, J., Vorosmarty, C., Saito, Y., Giosan, L., Nicholls, R.J., 2009. Sinking deltas due to human activities. Nature Geoscience 2(10), 681-686.

Tian, J.Y., 1997. Study on the effect of the drying up of the Yellow River on the ecological environment in the sea water near the delta. Marine Environmental Science 16 (3), 59-65 (in Chinese).

Vermote, E.F., ElSaleous, N., Justice, C.O., Kaufman, Y.J., Privette, J.L., Remer, L., Roger, J.C., Tanré, D., 1997. Atmospheric correction of visible to middle-infrared EOS-MODIS data over land surfaces: Background, operational algorithm and validation. Journal of Geophysical Research: Atmospheres 102, 17131-17141.

Wang, H.J., Bi, N.S., Saito, Y., Wang, Y., Sun, X.., Zhang, J., Yang, Z., 2010. Recent changes in sediment delivery by the Huanghe (Yellow River) to the sea: causes and environmental implications in its estuary. Journal of Hydrology 391(3-4), 302-313.

Wang, H., Wu, X., Bi, N., Li, S., Yuan, P., Wang, A., et al., 2017. Impacts of the dam-orientated water-sediment regulation scheme on the lower reaches and delta of the Yellow River (Huanghe): a review. Global & Planetary Change 157, 93-113.

Wang, H.J., Yang, Z., Saito, Y., Liu, J.P., Sun, X., Wang, Y., 2007. Stepwise decreases of the Huanghe (Yellow River) sediment load (1950-2005): impacts of climate change and human activities. Global and Planetary Change 57(3), 331-354.

Wang, W., Yi, H.P. Sun, Z.G., Wang, M.M., Lu, X.N., 2015. Impact of water and sediment regulation project implemented for 10 years on the trail channel and off-shore slope of Yellow River. Journal of Arid Land Resources and Environment 29(10), 86-92 (in Chinese).

Wu, X., Bi, N., Yuan, P., Li, S., Wang, H., 2015. Sediment dispersal and accumulation off the present Huanghe (Yellow River) delta as impacted by the water-sediment regulation scheme. Continental Shelf Research 111, 126-138.

Xu, H., 2006. Modification of normalised difference water index (NDWI) to enhance open water features in remotely sensed imagery. International Journal of Remote Sensing 27, 3025–3033.

Xu, J., 2008. Response of land accretion of the Yellow River delta to global climate change and human activity. Quaternary International 186(1), 4-11.

Xu, N., Gong, P., 2016. The impact of hurricane Katrina on the coastline west of New Orleans, USA. Chinese Science Bulletin 61(15), 1687-1694.

Yang, S.L., Milliman, J.D., Li, P., Xu, K., 2011. 50,000 dams later: Erosion of the Yangtze River and its delta. Global and Planetary Change 75, 14-20

Yu, J., Fu, Y., Li, Y., Han, G., Wang, Y., Zhou, D., Sun, W., Gao, Y., Meixner, F.X., 2011. Effects of water discharge and sediment load on evolution of modern Yellow River delta, China, over the period from 1976 to 2009. Biogeosciences 8(2), 2427-2435.

Yu, Y., Shi, X., Wang, H., Yue, C., Chen, S., Liu, Y., Hu, L., Qiao, S., 2013. Effects of dams on water and sediment delivery to the sea by the Huanghe (Yellow River): the special role of Water-Sediment Modulation. Anthropocene 3, 72-82.

Zang, Q.Y., 1996. Nearshore sediment along the Yellow River Delta. Ocean Press, Beijing.

Zhang, T.T., Zeng, S.L., Gao, Y., Ouyang, Z.T., Li, B., Fang, C.M., Zhao, B., 2011. Assessing impact of land uses on land salinization in the Yellow River delta, China using an integrated and spatial statistical model. Land Use Policy 28(4), 857-866.

Zhao, B., Guo, H., Yan, Y., Wang, Q., Li, B., 2008. A simple waterline approach for tidelands using multi-temporal satellite images: a case study in the Yangtze delta. Estuarine, Coastal and Shelf Science 77(1), 134-142.

Zhu, Q., Prooijen, B.C.V., Wang, Z.B., Yang, S.L., 2017. Bed-level changes on intertidal wetland in response to waves and tides: a case study from the Yangtze River delta. Marine Geology 385, 160-172.